2024 33rd International Conference on Computer Communications and Networks (ICCCN) | 979-8-3503-8461-1/24/$31.00 ©2024 IEEE | DOI: 10.1109/ICCCN61486.2024.10637535

# Super-resolution Localization and Tracking in WiFi Sensing

Jian Wang*, Jack Chuang*, Sebastian Semper†, and Nada Golmie*
*Wireless Networks Division, National Institute of Standards and Technology (NIST), USA
†Technische Universität Ilmenau, Institute for Information Technology, Ilmenau, Germany
Email: jian.wang@nist.gov, jack.chuang@nist.gov, Sebastian.Semper@tu-ilmenau.de, nada.golmie@nist.gov

***Abstract*—Integrated sensing and communication (ISAC) systems have been investigated by the research and standardization communities in the recent past. Accurately localizing the target and tracking the target's movement are critical for numerous smart Internet of Things (IoT) systems (smart manufacturing, smart transportation, etc.). This paper aims to realize super-resolution localization and tracking in WiFi sensing by leveraging the IEEE 802.11ad beamforming training procedure. We leverage the CLEAN-Space-Alternating Generalized Expectation-maximization (CLEAN-SAGE) algorithm on a single beam sweeping cycle for target localization and investigate the targets' delays and angle estimation. For tracking moving targets, we design mechanisms to estimate the target's motion, including the target's velocity and motion pattern, such as estimating the target's spatial positions over time to obtain the Doppler shift or tracking its trajectory using a Kalman filter. In order to prove that our approach works effectively, we conduct a thorough performance evaluation study. Our evaluation results confirm that the CLEAN-SAGE algorithm can achieve estimation performance beyond the ISAC system's inherent bandwidth and beamwidth constraints. Furthermore, we provide insights into how system configurations, including antenna size, beam overlap, and the number of iterations in the SAGE algorithm, influence its performance.**

***Index Terms*—Edge processing, IoT applications, mmWave, CLEAN and SAGE, WiFi sensing, Super-resolution algorithm, Localization and tracking**

## I. Introduction

The ability to accurately localize a target and continuously monitor the target's movement can enable numerous smart-world Internet of Things (IoT)-enabled applications [1]–[7]. For example, appliances and heating/cooling systems can adapt their functionalities in a smart home environment based on the occupants' position. In a smart manufacturing factory system, having timely information on the state (e.g., location and linear and angular velocity and acceleration) of the equipment and the personnel can significantly improve productivity and enhance safety. Likewise, vehicle localization and tracking are fundamental for autonomous driving vehicles to navigate safely in the intelligent transportation system.

Traditional methods for target localization and tracking rely on image sensors like cameras and other sensing modules like Light Detection and Ranging (LIDAR), and Radio Detection and Ranging (RADAR) [8]. Sensing with a camera or LIDAR may perform ineffectively in low-light or bad weather conditions. Using radar, although effective, entails additional costs for deployment. However, the ubiquitous deployment of the wireless communication infrastructure opens up new opportunities for sensing, including target positioning, which can be realized using commercial wireless communication signals employed in WiFi or 5G New Radio (NR) [9]. Sensing is envisioned to be an integral component of the next-generation wireless communication systems.

In addition to using a shared waveform to improve spectrum usage, integrated sensing and communication (ISAC) can reduce operational costs by sharing several vital components, including the system's Radio Frequency (RF) front ends and signal processing modules [1]. In particular, channel estimation is essential in a wireless communication system. The pilot signal arrived at the receiver can be utilized to estimate the channel characteristics and compensate for the channel's impact on the communication signals. Additionally, channel estimation results can be used for target detection and tracking. This is vital because the presence and movement of the target will lead to changes in the propagation channels.

The conventional method of locating a target uses a known pilot signal to identify the delay shift of the received pilot, which corresponds to the peak power in the matched filter output. In particular, the pilot symbols inside an Orthogonal Frequency Division Multiplexing (OFDM) waveform are employed for radar sensing by combining the matched filter detection with the 2D Fourier transform for velocity estimation [10]. Similarly, Golay complementary sequences, the preamble in the IEEE 802.11ad waveform, are leveraged to realize automotive radar by leveraging Channel Impulse Responses (CIRs) obtained from channel estimation [11]. Meanwhile, the angle to the target is derived from the steer direction of the beam that yields the maximum received power. Thus, the bandwidth and beamwidth can limit the sensing performance.

To overcome the limitations of system bandwidth and beamwidth, super-resolution algorithms are vital solutions for improving detection resolutions. Super-resolution algorithms can achieve a high-precision estimation of multiple target parameters, including range, angle, and Doppler frequency shift. Some commonly used super-resolution algorithms, including MUltiple SIgnal Classification (MUSIC) and Estimation of Signal Parameters through Rotational Invariance Techniques (ESPRIT), are subspace methods. These methods achieve signal detection by separating signal space and noise space, and Space Alternating Generalized Expectation-maximization

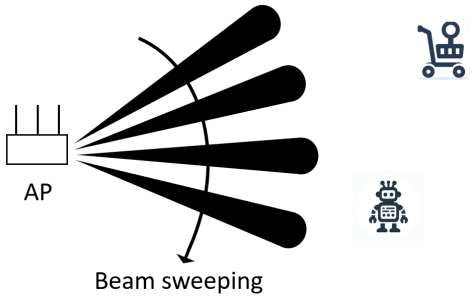


Fig. 1. Beam sequentially sweeps in a clockwise direction to cover a designated area

(SAGE) and CLEAN are greedy methods based on maximizing the likelihood function. Several research efforts [12], [13] investigated subspace methods in detail, performing parametric estimation on delay, angle, and Doppler. For example, in [12], a MUSIC-based algorithm was applied to the OFDM integrated radar and communication waveform to lead to a super-resolution range and Doppler estimation. Likewise, MUSIC algorithms were adopted for the multipath components (MPCs) detection and estimation in a WiFi opportunistic sensing scenario [13]. In addition, the MUSIC algorithm was adopted to overcome the limitation of the spatial resolution in a commercial 60 GHz WiFi system, enabling RF imaging [14]. The performance of the subspace-based algorithms declines significantly in low Signal-to-Noise Ratio (SNR) conditions, and the estimation of the number of targets can substantially affect the overall estimation results. The CLEAN-SAGE algorithm is a vital solution to overcome these limitations.

This study utilizes the IEEE 802.11ad beamforming training procedure. The key contributions of our work are as follows: (i) We adapt the CLEAN-SAGE algorithm to estimate the target's delay and angle in a single beam sweeping cycle. (ii) We extend the CLEAN-SAGE estimation into the time dimension to estimate target motion based on the results obtained from multiple continuous CLEAN-SAGE observations of beam-sweeping cycles. (iii) We provide some insights into how system configurations, such as the antenna array size, beam overlap, and the number of iterations in the SAGE algorithm, impact the evaluation performance.

The remainder of the paper is organized as follows: Section II introduces the system, channel, and signal models. Section III presents our proposed approach for realizing super-resolution in WiFi sensing. Section IV provides the performance evaluation results to demonstrate the effectiveness of our approach. Finally, Section V concludes the paper.

## II. System, Channel, and Signal Models

### A. System Model

To fulfill the link budget requirement, directional communication is vital for high-frequency communication, such as in the mmWave or terahertz frequency bands. To ensure the beams of the transmitter and the receiver are effectively aligned, beamform training and periodic beam refinement are essential procedures that are realized through beam sweeping. During the beam sweeping, the coverage area is divided into a set of sectors with equal size, and the access point (AP) or station (STA) transmits over each sector sequentially, as shown in Fig. 1. At the beginning of each beacon interval (BI), i.e., a superframe in IEEE 802.11ad, AP sends network announcements and performs beamform training. To do that, a control PHY (CPHY) packet is transmitted at each sector. The preamble within the CPHY is used to estimate the channel. In every CPHY packet, the preamble includes a short training field (STF) and a channel estimation field (CEF). The STF is for detecting frame start, while the CEF consists of complementary Golay sequences for estimating the channel. The preamble has 59 Golay sequences in total, with each Golay sequence comprising 128 symbols. The details regarding performing channel impulse response (CIR) estimation using the preamble can be found in [12]. The BI duration is configurable with a typical value of 100 ms.

In this study, we explore the feasibility and effectiveness of using periodically steered beams for sensing tasks such as surveillance. In particular, we investigate the target localization performance and how it can be impacted by system configurations, including beam width, beam overlapping ratio, and BI values.

Our system model adopts a monostatic configuration in which both transmitter and receiver are deployed at the AP. The AP operates in a full-duplex mode, enabling simultaneous transmission and reception, which is motivated by recent advances in full-duplex wireless communications [15]. Specifically, the AP transmits CPHY sequentially at each sector while concurrently, the sensing receiver carries out radar functionality by observing the received signal, which may be reflected off targets.

For the beamform training scenario, where the beam is steered along the azimuth angle, we examine a uniform linear array (ULA), which possesses $M$ antennas spaced at half wavelength distance. The goal is to accurately estimate the azimuth angles of the Multipath Components (MPCs), which are individual reflections from objects in the environment. Given that the scenarios are Line-of-Sight (LoS) and in a far-field context, the Angle of Arrival (AoA) is equivalent to the Angle of Departure (AoD).

### B. Channel Model

Channel model $\mathbf{H}(t, \boldsymbol{g}, \boldsymbol{\tau}, \boldsymbol{\theta})$, which is a function of time $t$, path gains $\boldsymbol{g}$, delays $\boldsymbol{\tau}$, and azimuth angles $\boldsymbol{\theta}$ can be defined by,

$$\boldsymbol{H}(t, \boldsymbol{g}, \boldsymbol{\tau}, \boldsymbol{\theta}) = \sum_{l=1}^{L} g_l e^{-j2\pi f_c \tau_l} \delta(t - \tau_l) \mathbf{a_r}(\theta_l) \mathbf{a_t}(\theta_l)^H, \quad (1)$$

Here, $L$ is the number of MPCs, and $g_l$ is the $l$-th path's complex gain. The term $e^{-j2\pi f_c \tau_l}$ models the phase shift introduced by the carrier frequency $f_c$ and the path delay $\tau_l$. The function $\delta(t - \tau_l)$ is the Dirac delta function, indicating the arrival time $\tau_l$ of the $l$-th path at the receiver. The vectors

$\mathbf{a_r}(\theta_l)$ and $\mathbf{a_t}(\theta_l)$ represent the antenna array response of the $l$-th path at the receiver and transmitter, respectively, and $\boldsymbol{x}^H$ is the conjugate transpose of the complex-valued vector $\boldsymbol{x}$.

In one sector-level sweep (SLS) phase, in order to cover the entire area, the AP sequentially directs its signal toward specific directions. The array response vector $\mathbf{a}(\theta)$ can be described as: $\mathbf{a}(\theta) = \frac{1}{\sqrt{M}}[1, e^{\jmath\pi\sin\theta}, e^{\jmath 2\pi\sin\theta}, \cdots, e^{\jmath(M-1)\pi\sin\theta}]$, where $M$ and $\theta$ stand for the number of antenna elements in the ULA, and the azimuth angle of a propagation path, respectively.

We assume the same ULA with $M$ antenna elements is used at the transmitter and the sensing receiver, i.e., $\mathbf{a_t}(\theta) = \mathbf{a_r}(\theta) = \mathbf{a}(\theta)$. Furthermore, the transmitter and the sensing receiver are steered in the same direction, such as, at the $k$-th sector. After applying beam steering vectors $\mathbf{a}(\theta_k)$ to the channel matrix $\mathbf{H}(t, \boldsymbol{g}, \boldsymbol{\tau}, \boldsymbol{\theta})$, a tap-delay channel response will be obtained by

$$\mathbf{h}_{\theta_k}(t,\tau) = \mathbf{a}(\theta_k)^H \mathbf{H}(t, \boldsymbol{g}, \boldsymbol{\tau}, \boldsymbol{\theta}) \mathbf{a}(\theta_k), \tag{2}$$

$$= \sum_{l=1}^{L} \alpha_l(\theta_k, \theta_l) e^{j2\pi f_c \tau_l} \delta(t - \tau_l). \tag{3}$$

Here, the path gain after beamforming can be represented as $\alpha_l(\theta_k, \theta_l) = g_l \mathbf{a}(\theta_k)^H \mathbf{a}(\theta_l) \mathbf{a}(\theta_l)^H \mathbf{a}(\theta_k)$.

### C. Signal Model

The transmission signal, i.e., an SLS data package, includes a pilot sequence of length $L_s$ and can be characterized as follows:

$$s(t) = \sqrt{E_s} \sum_{m=0}^{L_s - 1} b(m) p(t - mT_s). \tag{4}$$

Here, $b(m)$ is the symbol after $\frac{\pi}{2}$-BPSK modulation, where $b(m) \in \{1, -1, i, -i\}$, $E_s$ is the energy of a symbol, and $p(\cdot)$ is the pulse shaping function applied to each symbol.

At the receiver, for each steering angle $\theta_k$, the received signal $r(t, \theta_k) = s(t) * \mathbf{h}_{\theta_k}(t, \tau) + w(t)$ can be formulated as the $L$ delayed copies of the transmit signal via the $L$ propagation paths, plus the receiver's thermal noise. Then, we have

$$r(t, \theta_k) = \sum_{l=0}^{L-1} \alpha_l(\theta_k, \theta_l) e^{j(2\pi f_c \tau_l)} s(t - \tau_l) + w(t). \tag{5}$$

Here, denote $w(t) \sim \mathcal{CN}(0, \sigma_w^2)$ as a complex circularly-symmetric Gaussian random variable.

From the received signal $r(t, \theta_k)$, we can get the estimated channel CIR $\widehat{\mathbf{h}}_{\theta_k}(t, \tau)$ via frame detection and channel estimation based on the detected pilot signal [12]. After transmitting a CPHY data packet in a sector, the transmitter will switch to the next sector and transmit a new CPHY packet. The waveform, as described in Eqn. (5), will then be received from the new steering angle $\theta_k'$, and its corresponding CIR, denoted as $\widehat{\mathbf{h}}_{\theta_k'}(t, \tau)$ or $\{\hat{\mathbf{h}}(\theta_k')\}$, will be computed. During each SLS, the transmitter navigates through $K$ predefined steer directions, and the CIRs $\{\hat{\mathbf{h}}(\theta_k)\}_{k=1}^K$ will be collected. We denote matrix $\hat{\mathbf{H}}_s$ as $\hat{\mathbf{H}}_s = [\hat{\mathbf{h}}(\theta_1), \hat{\mathbf{h}}(\theta_2), \cdots, \hat{\mathbf{h}}(\theta_K)]$, which contains the estimated CIRs for all $K$ steering angles.

By leveraging the SLS procedure, the AP can track the changes continuously in a coverage area or follow the movement of the target. In our analysis, we consider a slow-changing system, where the path gain $\alpha_l(\theta_k, \theta_l)$, angle $\theta_l$, and delay $\tau_l$ remain constant within a single SLS. The SLS typically lasts on the order of one-tenth of a millisecond.

## III. Supper-Resolution Approach

### A. Design Rationale

MPC parameter estimation is performed by aggregating the CIRs obtained at each steer direction during a complete sweep into the estimated CIR matrix $\hat{\mathbf{H}}_s$. Recall the default delay and angle estimation resolution, limited by the signal bandwidth and system beamwidth, often falls short for specific IoT applications, such as multi-object tracking, where finer spatial resolution is required. To address these challenges, we explore the SAGE algorithm [16], an iterative method for refining parameters, combined with the CLEAN algorithm [17], which provides an initial estimation for SAGE, to achieve super-resolution estimation. This CLEAN-SAGE algorithm is applied directly on $\hat{\mathbf{H}}_s$.

For moving targets, beyond accurate localization, it is equally important to estimate and monitor their movements, including estimating the targets' instantaneous velocity vectors and discerning their motion patterns, which is essential to support a multitude of IoT applications. To estimate motion, the traditional method in radar applications is to perform Doppler estimation to obtain the moving target's radial velocity. To accurately observe phase changes and estimate Doppler, the signal has to be sampled at least at the Nyquist sampling rate, which can be challenging, especially for a high-frequency communication system operating in the mmWave or TeraHertz frequency band. To mitigate these challenges, for applications with smooth motion, we investigate the feasibility of observing the channel at a sub-Nyquist rate and using spatial information, such as delay and angle, to track and predict the motion of the targets.

In the following, we begin with outlining the SAGE-CLEAN algorithm, which estimates the object's angle and delay. Subsequently, we explore leveraging the spatial locations of the object over time to accurately estimate the Doppler frequency shift using the Best Linear Unbiased Estimator (BLUE). Additionally, we investigate object tracking and localization using the Extended Kalman Filter (EKF).

### B. Angle and Delay Estimation

We now describe in detail how the CLEAN-SAGE algorithm is used to estimate the set of delays and angles of $L$ MPCs, i.e., $\{\hat{\tau}_l, \hat{\theta}_l\}_{l=1}^L$, during an SLS cycle.

The CLEAN-SAGE algorithm is an iterative operation. The CLEAN algorithm is greedy and will find the most dominant path in the CIR matrix. The estimated path using CLEAN will serve as the initial value and will be further refined using the SAGE algorithm. In general, for both CLEAN and SAGE, the

estimation of $\hat{\tau}_l$ and $\hat{\theta}_l$ is performed through a grid search. We denote the grid resolutions as $\Delta\tau$ and $\Delta\theta$, which will become finer with each SAGE iteration. The objective of the search is to find the optimum value of $\hat{m}$ and $\hat{n}$, such that $\hat{n}\Delta\theta$ and $\hat{m}\Delta\tau$ maximize the likelihood between the reconstructed path responses and the CIR matrix, denoted as $\hat{\mathbf{H}}$, the angle estimation and the subsequent delay estimation are detailed in Equations (6) and (7). Note that the dimensions of the matrix $\hat{\mathbf{H}}$ are equal to the number of symbols $L_s$ multiplied by the number of steer directions $K$. The range of $\hat{m}$ and $\hat{n}$ for this search extends from 1 to $M$ and 1 to $N$, respectively.

$$\hat{n} = \arg\max_{n} \frac{\left\|\hat{\mathbf{H}}\mathbf{u}_n\right\|}{\left\|\hat{\mathbf{H}}\right\| \|\mathbf{u}_n\|}, \tag{6}$$

$$\hat{m} = \arg\max_{m} \frac{\left\|\mathbf{v}_m^H \hat{\mathbf{H}}\mathbf{u}_{\hat{n}}\right\|}{\|\mathbf{v}_m\| \left\|\hat{\mathbf{H}}\mathbf{u}_{\hat{n}}\right\|}, \tag{7}$$

Reconstructed angle response vector $\mathbf{u}_n$ for MPC angle $n\Delta\theta$ at all $\{k\}_{k=1}^{K}$ steering directions can be computed via

$$\mathbf{u}_n(k) = \mathbf{a}(\theta_k)^H \mathbf{a}(n\Delta\theta)\mathbf{a}(n\Delta\theta)^H \mathbf{a}(\theta_k), \tag{8}$$

and the delay response vector $\mathbf{v}_m$ for a delay value $m\Delta\tau$, with $\{q\}_{q=1}^{L_s}$, can be constructed by

$$\mathbf{v}_m(q) = e^{-j2\pi f_c m\Delta\tau} p(qT_s - m\Delta\tau), \tag{9}$$

where $p(t) = s(t) * s(-t)$ is the matched filter output of the transmit signal. Once we obtain the estimated delay and angle for a MPC, its complex gain $\hat{g}_{(\hat{m},\hat{n})}$ can be obtained by solving $(\mathbf{v}_{\hat{m}} \otimes \mathbf{u}_{\hat{n}}) g_{(\hat{m},\hat{n})} = \text{vec}(\hat{\mathbf{H}})$, using the least-squares method, where $\otimes$ is the Kronecker product of the two vectors and $\text{vec}(\cdot)$ is the vectorization operation, stacking the columns of $\hat{\mathbf{H}}$.

At every iteration of the CLEAN operation, it tries to locate the most dominant path. With $P$ most dominant paths detected, the delays, angles, and complex amplitudes $\{\hat{\tau}_p, \hat{\theta}_p, \hat{g}_p\}_{p=1}^{P}$ are aggregated to reconstruct the channel response as follows:

$$\mathbf{H}_P = \sum_{p=1}^{P} \mathbf{H}(\hat{\theta}_p, \hat{\tau}_p), \tag{10}$$

with

$$\mathbf{H}(\hat{\theta}_p, \hat{\tau}_p) = \hat{g}_l \mathbf{v}_{\hat{\tau}_p}((\mathbf{A}_s^H \mathbf{a}(\hat{\theta}_p)) \circ (\mathbf{A_s}^H \mathbf{a}(\hat{\theta}_p)))^H,$$

where $\circ$ is the Hardamard product, $\mathbf{A}_s$ represents the steering matrix, defined as $\mathbf{A}_s = [\mathbf{a}(\theta_1), \mathbf{a}(\theta_2), \ldots, \mathbf{a}(\theta_K)]$, with each column $\mathbf{a}(\theta_k)$ corresponding to the steering vector at angle $\theta_k$. The residual matrix $\mathbf{R}$ is computed by the subtraction of $\mathbf{H}_P$ from the channel matrix $\hat{\mathbf{H}}$.

With the initial MPC estimation provided by CLEAN, SAGE performs iterative expectation maximization (E-M) processes to further refine $\hat{g}$, $\hat{\theta}$, and $\hat{\tau}$. The refinement is carried out on each MPC $l$ in the set of the $P$ most dominant paths. The path response of the $l$-th MPC is computed as:

$$\mathbf{H}_{\text{res},l} = \mathbf{R} + \mathbf{H}(\hat{\theta}_l, \hat{\tau}_l), \tag{11}$$

In the SAGE algorithm, detailed in Algorithm 1, angle and delay are sequentially refined, i.e., the angle is refined with a fixed delay value and vice versa. SAGE is an iterative operation consisting of the expectation (E) and maximization (M) steps. For each iteration, the new search grid resolution $\Delta\theta^i$ and $\Delta\tau^i$ reduce to a fraction of the previous values. The search is accomplished around the current estimated value $\hat{\theta}^{i-1}$ and $\hat{\tau}^{i-1}$. For example, for the $i$-th iteration, the candidate parameters are updated to $\{\hat{\theta}^{i-1} + m\Delta\theta^i\}_{m=1}^{M^i}$ and $\{\hat{\tau}_l^{i-1} + n\Delta\tau^i\}_{n=1}^{N^i}$. Here, $M^i$ and $N^i$ define the search space for the $i$-th iteration.

The workflow of the combined CLEAN and SAGE algorithm is described in Algorithm 2. The parameters of the most dominant path in the CIR matrix is first estimated using CLEAN. Subsequently, the parameters of the detected MPCs are refined by SAGE. Finally, the impact of the estimated paths will be subtracted from the CIR matrix, based on the refined parameters, to obtain the CIR matrix residual. The CLEAN algorithm will again apply to the CIR residual to extract the following most dominant path and add it to the detected MPC list. This operation repeats until the detected number of MPCs reaches a predefined number or some stopping criteria have been met, such as the energy of the residual MPCs has dropped below a certain threshold.

**Algorithm 1:** Space Alternating Generalized Expectation-maximization (SAGE)

**Input:** Initial parameter estimation of the $P$ most dominant MPCs, residual CIR matrix $\boldsymbol{R}$, number of SAGE iterations
**Output:** Refined MPC parameters
**for** each detected MPC $l$ **do**
  Compute $\mathbf{H}_{\text{res},l}$ by adding the $l$-th path response $\mathbf{H}(\hat{\theta}_l, \hat{\tau}_l)$ back to $\boldsymbol{R}$ (Equation (11))
  *E-Step for Angle Estimation:* Compute angle expectation based on current delay estimate $\hat{\mathbf{h}}_{\hat{\tau},l} = \mathbf{H}_{\text{res},l}^H \mathbf{v}_{\hat{\tau}_l}$
  **for** each SAGE iteration $i$ **do**
    Refine search resolution by updating $\Delta\theta^i$, and define the search region around current estimation $\hat{\theta}_l^{i-1}$
    *M-Step for Angle Estimation:* Maximize the likelihood function to update $\hat{\theta}_l^i = \hat{\theta}_l^{i-1} + \hat{n}^i\Delta\theta^i$, such that
    $\hat{n}^i = \arg\max_{n^i} \frac{\left\|\hat{\mathbf{h}}_{\hat{\tau},l}^H \mathbf{u}_{n^i}\right\|}{\left\|\hat{\mathbf{h}}_{\hat{\tau},l}\right\| \left\|\mathbf{u}_{n^i}\right\|}$
  **end for**
  *E-Step for Delay Estimation:* Compute delay expectation based on current angle estimate $\hat{\mathbf{h}}_{\hat{\theta},l} = \mathbf{H}_{\text{res},l}\mathbf{u}_{\hat{\theta}_l}$
  **for** each SAGE iteration $i$ **do**
    Refine the search resolution $\Delta\tau^i$, and define the search area around current estimation $\hat{\tau}_l^{i-1}$
    *M-Step for Delay Estimation:*Maximize the likelihood function to update $\hat{\tau}_l^i = \hat{\tau}_l^{i-1} + \hat{m}^i\Delta\tau^i$, such that
    $\hat{m}^i = \arg\max_{m^i} \frac{\left\|\hat{\mathbf{h}}_{\hat{\theta},l}^H \mathbf{v}_{m^i}\right\|}{\left\|\hat{\mathbf{h}}_{\hat{\theta},l}\right\| \left\|\mathbf{v}_{m^i}\right\|}$
  **end for**
  Update the complex path gain $\hat{g}_l$ with updated angle and delay
  Update the residual $R$ by subtracting the $l$-th path response
**end for**
**return** Refined MPC parameters

**Algorithm 2:** CLEAN-SAGE Algorithm for Multipath Component Estimation

**Input:** CIR matrix for $K$ steering directions $\hat{\mathbf{H}}_s$, grid resolution $\Delta\theta$ and $\Delta\tau$, number of paths to estimate $L$, the number of iterations for SAGE algorithm

**Output:** Estimated angles $\hat{\theta}$, delays $\hat{\tau}$, gains $\hat{g}_{(\hat{\theta},\hat{\tau})}$ for detected paths, and residual CIR matrix

Initialize residual CIR matrix $\mathbf{R}$ to $\hat{\mathbf{H}}_s$

Compute response matrices $\mathbf{U}$ and $\mathbf{V}$ using Equation (8) and Equation (9)

**while** Energy of the last detected path is smaller than a predefined threshold and number of detected paths $P$ is less than $L$ **do**

Estimate parameters of the most dominant path using Eqn. (6) and Eqn. (7)

Refine the parameters of the detected MPCs using the SAGE algorithm described in Algorithm 1

Update residual CIR matrix $\mathbf{R}$ by subtracting the path responses, computed per Eqn. (10), from $\hat{\mathbf{H}}_s$

**end while**

**return** Estimated angles $\hat{\theta}$, delays $\hat{\tau}$, gains $\hat{g}_{(\hat{\theta},\hat{\tau})}$ for each path, and final residual CIR matrix $\mathbf{R}$

### C. Motion Estimation

In the following, we first detail the Doppler estimation based on the complex gain and delay obtained using the aforementioned CLEAN-SAGE algorithms by leveraging the BLUE algorithm [18]. We then demonstrate target localization and tracking for motion analysis using EKF prediction and tracking [18].

*1) Doppler Frequency Estimation:* A series of observations are required to estimate the Doppler frequency shift $f_d$ for a given MPC. We assume $N_d$ samples at sampling time $\{t_i\}_{i=1}^{N_d}$ were collected with $\Delta t$ time gap in between. The Doppler frequency shift can be extracted through the signal phase change over the observation period. The complex gain of the MPC at time $t_i$, after taking its path delay $\tau_l$ at $t_i$ into account, can be computed as $c_i(l,\tau_l) = \alpha(l,\tau_l)e^{j2\pi f_c \tau_l}$, and its phase $\theta(l,i) = \angle c_i(l,\tau_l) = 2\pi f_d t_i + w_i$, where $w_i$ is the measurement noise with zero mean and variance $\sigma^2$ is uncorrelated between the measurements.

Considering the phase rotation between two consecutive samples, we can construct $\mathbf{x}$ with its element as: $x(i-1) = \theta(i) - \theta(i-1) = 2\pi f_d(t_i - t_{i-1}) + w_i - w_{i-1} = 2\pi f_d \Delta t + n(i)$.

Assuming the Doppler frequency shift is a constant value over the observation duration, which is a sufficiently short duration in the order of several milliseconds, the corresponding Doppler frequency shift of the reflection path is estimated using the BLUE as:

$$\hat{f}_d = \frac{\mathbf{s}^T\mathbf{C}^{-1}\mathbf{x}}{\mathbf{s}^T\mathbf{C}^{-1}\mathbf{s}}, \tag{12}$$

where $\mathbf{s} = [2\pi\Delta t, 2\pi\Delta t, \cdots, 2\pi\Delta t]^T$, and the covariance matrix $\boldsymbol{C}$ is

$$\mathbf{C} = \mathbb{E}[(\mathbf{x} - \mathbb{E}(\mathbf{x})(\mathbf{x} - \mathbb{E}(\mathbf{x})^T)] = \sigma^2\mathbf{U}\mathbf{U}^T$$

where

$$\mathbf{U} = \begin{bmatrix} 1 & -1 & & \\ & 1 & \ddots & \\ & & \ddots & -1 \\ & & & 1 \end{bmatrix}$$

Thus, $\hat{f}_d$ can be simplified as:

$$\hat{f}_d = \frac{\mathbf{s}^T(\mathbf{U}\mathbf{U}^T)^{-1}\mathbf{x}}{\mathbf{s}^T(\mathbf{U}\mathbf{U}^T)^{-1}\mathbf{s}}. \tag{13}$$

*2) Objects Localization and Tracking:* To monitor the motion of multiple targets, we need three key steps: (i) predict the target spatial positions for the forthcoming time instance, (ii) associate the predicted positions with the actual observations, and (iii) use the matched measurements to refine the existing predictions.

In our study, the prediction is carried out by leveraging the Kalman Filter. Denote the state vector at time $t_k$ as $\mathbf{s}(k) = [x(k), v_x(k), y(k), v_y(k)]^T$, encompassing the x-coordinate, $x$-direction's velocity, $y$-coordinate, and $y$-direction's velocity, respectively, with the state transition described as:

$$\mathbf{s}(k) = \mathbf{A}\mathbf{s}(k-1) + \mathbf{B}\mathbf{u}(k). \tag{14}$$

Here, $\mathbf{A}$ and $\mathbf{B}$ are the state transition matrix and the control input matrix to consider the random disturbance in the system respectively. $\mathbf{u}(k) = [0, u_{v_x}(k), 0, u_{v_y}(k)]^T$ represents control input vector. The driving noises, $u_{v_x}$ and $u_{v_y}$, follow independent normal distribution $N(0, \sigma_{v_x}^2)$ and $N(0, \sigma_{v_y}^2)$, respectively.

The observation vector, denoted as $\mathbf{x}(k) = [r(t), \theta(t)]^T$, comprises the target's range and angle, which can be derived from the state vector as follows:

$$\mathbf{r}(k) = \sqrt{x(k)^2 + y(k)^2} + w_r(k) \tag{15}$$

$$\theta(k) = \frac{\pi}{4} - \arctan\frac{y(k)}{x(k)} + w_\theta(k), \tag{16}$$

where $w_r$ and $w_\theta$ are independent observation noises, which are Gaussian variables with zero mean and

$$\mathbb{E}(\mathbf{w}(k_1)\mathbf{w}(k_2)^T) = \begin{bmatrix} \sigma_{w_r}^2 & 0 \\ 0 & \sigma_{w_\theta}^2 \end{bmatrix}\delta(k_1 - k_2),$$

where $\mathbf{w}(k) = [w_r(k), w_\theta(k)]^T$. Note that the $0^\circ$ observation angle corresponds to the $45^\circ$ angle in the x-y coordinates to match the antenna orientation in the next evaluation section.

Because of the non-linearity of the observation functions, an extended Kalman filter is used to predict the target's motion. After linearizing Eqn. (15) and Eqn. (16), the observation matrix becomes time-variant and is written as

$$\begin{bmatrix} r(k) \\ \theta(k) \end{bmatrix} = C(k)\begin{bmatrix} x(k) \\ v_x(k) \\ y(k) \\ v_y(k) \end{bmatrix} + \begin{bmatrix} w_r(k) \\ w_\theta(k) \end{bmatrix} \tag{17}$$

$$C(k) = \begin{bmatrix} \frac{x(k)}{\sqrt{x^2(k)+y^2(k)}} & 0 & \frac{y(k)}{\sqrt{x^2(k)+y^2(k)}} & 0 \\ \frac{y(k)}{x^2(k)+y^2(k)} & 0 & -\frac{x(k)}{x^2(k)+y^2(k)} & 0 \end{bmatrix} \tag{18}$$

Therefore, the state error covariance matrix and the observation error covariance matrix are

$$\mathbf{P} = \begin{bmatrix} 0 & 0 & 0 & 0 \\ 0 & \sigma_{v_x}^2 & 0 & 0 \\ 0 & 0 & 0 & 0 \\ 0 & 0 & 0 & \sigma_{v_y}^2 \end{bmatrix}$$

$$\mathbf{D} = \begin{bmatrix} \sigma_{w_r}^2 & 0 \\ 0 & \sigma_{w_\theta}^2 \end{bmatrix}$$

With the initial state $\mathbf{s}[-1|-1]$ and the initial prediction MSE $\mathbf{M}[-1|-1]$), the prediction and tracking procedure involves the following steps: (i) Predict the state by updating the state estimate from the previous time step using $\mathbf{s}[k|k-1] = \mathbf{A}\mathbf{s}[k-1|k-1]$, where $\mathbf{s}[k|k-1]$ indicates the predicted $\mathbf{s}[k]$ based on the measurements from $t_0$ to $t_{k-1}$. (ii) Calculate the minimum prediction MSE matrix by $\mathbf{M}[k|k-1] = \mathbf{A}\mathbf{M}[k-1|k-1]\mathbf{A}^T + \boldsymbol{P}$. (iii) Update the Kalman Gain matrix by $\mathbf{K}[k] = \mathbf{M}[k|k-1]\mathbf{C}^T(k)(\boldsymbol{D}+\mathbf{C}(\mathbf{K})\mathbf{M}[k|k-1]\mathbf{C}^T(k))^{-1}$. (iv) Compute the predicted measurement at time $k$, $\hat{\mathbf{x}}(k)$, based on Eqn. (15) and Eqn. (16) and associated each predicted value $\hat{x}_i$ with an observation $x_i$. In particular, find the assignment $\{x_i\}_{i=1}^n$ which satisfies $\min \sum_{\hat{\mathbf{x}}_i} d(\hat{\mathbf{x}}_i, \mathbf{x}_i)$, where $d(\cdot)$ is the Euclidean distance between a corresponding pair of vectors. (v) State correction based on the associated observations via $\mathbf{x}(k)$ via $\hat{\mathbf{s}}[k|k] = \hat{\mathbf{s}}[k|k-1] + \mathbf{K}(k)(\mathbf{x}(k) - \hat{\mathbf{x}}(k))$. (vi) Update the minimum prediction MSE matrix via $\mathbf{M}[k|k] = (\mathbf{I} - \mathbf{K}(k)\mathbf{C}(k))\mathbf{M}[k|k-1]$.

## IV. Performance Evaluation

### A. Methodology

Our simulation employs a monostatic configuration with a co-located transmitter and receiver at the AP. Sufficient RF isolation is considered between the transmitter and receiver, which enables the AP to operate in full-duplex mode. Without loss of generality, both transmitter and receiver use the same ULA antennas, with half wavelength spacing between antenna elements. A Kaiser window with a shape factor of 3.4 is applied to suppress the sidelobe of the beam pattern.

Our evaluation scenario consists of one AP, which is located at $x = 0$ and $y = 0$; this is the origin of our coordinate system, which is located in a corner of a room of size 7 m $\times$ 7 m. The transmitter and receiver antennas are oriented towards the room, with their boresight directed at a $45^\circ$ angle from the x-axis. Targets are randomly dropped into the area and move following a Gaussian Markov process described by Equation (14) for state transition. Without loss of generality, we assume point targets in our evaluation, allowing the terms "target" and "MPC" to be interchangeable in our discussion. Each target moves with a speed uniformly distributed between 0 m/s and 0.6 m/s, in a direction uniformly distributed between 0 radians and $2\pi$ radians. Upon reaching the room's boundary, the target will reflect off the boundary, with the reflection angle equal to the incident angle, and continue to move. Furthermore, the target reflection intensity is inversely proportional to the fourth power of the target range as given by the point target radar range equation.

The observation vectors $[\mathbf{r}(k), \theta(k)]^T$, defined in Eqn. (15) and Eqn (16), are obtained via CLEAN-SAGE estimation. The surveillance area covers 2 m $\leq x \leq$ 7 m and 2 m $\leq y \leq$ 7 m, which is the shaded area in the room, shown as Fig. 3. The configuration tends to avoid the situation that some targets are significantly closer to the AP than other targets, thereby introducing much stronger reflection path gain and overpowering the reflections from other targets. This also indicates that multiple APs may be required to monitor the activities in a room collaboratively. For this study, we focus on a single AP and leave the collaboration of multiple APs for our future study.

The definition of SNR is SNR $= E_s M^2/\sigma^2$, where $E_s$ is the energy of the transmit symbol, $M$ is the number of antenna elements of the ULA, and $\sigma^2$ is the variance of the complex Gaussian noise at the receiver.

In the coverage area (shaded area in Fig. 3), we have randomly deployed a number of targets. The AP transmits the CPHY signal, which hits the targets and then scatters back to the receiver. The delay, angle, and Doppler frequency shift will be estimated using the back-scattered CPHY signal. The performance metrics are defined as follows: for angle and delay, we use root mean square error (RMSE) to compare the ground truth with the estimated value, such that $\text{RMSE}_\theta = \sqrt{\mathbb{E}[(\theta - \hat{\theta})^2]}$ and $\text{RMSE}_\tau = \sqrt{\mathbb{E}[(\tau - \hat{\tau})^2]}$. For Doppler frequency or velocity estimation, we adopt the mean absolute error (MAE) between the ground truth and the estimation, for example, $\text{MAE}_{f_d} = \mathbf{E}[|f_d - \hat{f}_d|]$. We assume the number of targets is known in our evaluation.

Considering motion estimation, we first show the estimation results using the BLUE algorithm based on the signal phase obtained using the SAGE algorithms. To monitor the phase changes of target reflection, the observation interval is required to be at a maximum value of 2.08 ms, which can introduce significant overhead for the WiFi communication. To address this challenge, we demonstrate target localization and tracking using a sub-Nyquist sampling interval of 300 ms.

### B. Results

*1) Delay, Angle, and Doppler Estimation:* We begin with evaluating the range, delay, and angle estimation performance for one target in the designated area. Fig. 2 compares the estimation performance for two antenna configurations, i.e., 8-element ULA and 16-element ULA across different SNR levels. The performance is displayed as the logarithm of the range RMSE, the angle RMSE, and the Doppler MAE. The error medians are indicated by the central line within each box, while the bottom edges and top edges show the 5-th and 95-th percentiles, respectively. As seen in the figure, the general trend shows the estimation errors decline as SNR grows. However, the performance improvements for range and Doppler estimation diminish as SNR increases, which is expected as the range estimation mainly depends on the signal bandwidth, and the Doppler estimation relies on the accurate

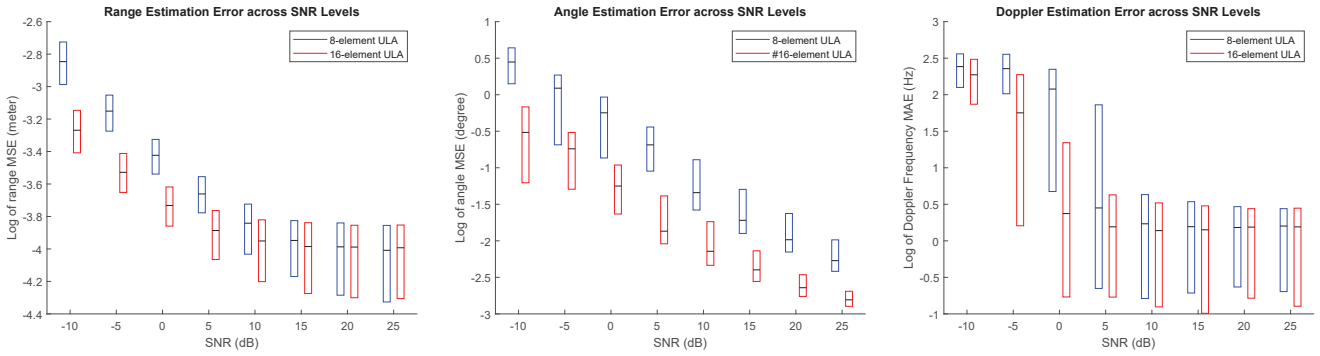


(a) (b) (c)

Fig. 2. Impact of Antenna size on estimation accuracy, measured across a range of SNR levels, with bars indicating 5th to 95th percentiles. The estimation error is measured using the SAGE-CLEAN algorithm for 8-element and 16-element ULAs. The beam gap is 65% of the beam width, with one target randomly distributed in the designated area. (a) Range Estimation Error (b) Angle Estimation Error, and (c) Doppler Estimation Error.

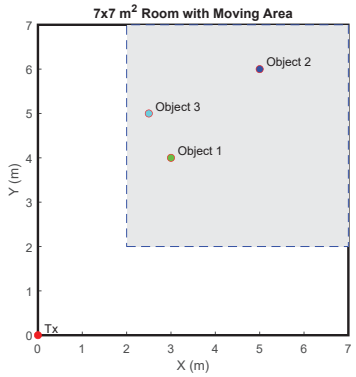


Fig. 3. Room

detection of the target range. Furthermore, the improvement is particularly notable for angular estimation, where the 16-element ULAs constantly demonstrate better estimation accuracy and precision than the 8-element ULAs across all SNR values due to its narrower beam and more steer directions leading to higher angular resolution. Note that the Doppler is estimated using a sampling interval of 1 ms and an observation length of 20 samples.

To understand how the number of iterations could impact the algorithm performance, we demonstrate the detection performance across different SNRs, as shown in Fig. 4. The central line in each box indicates the median error, and the bottom and top edges of the box indicate the 5-th and 95-th percentiles of the error. The boxes of different colors represent various numbers of iterations employed in the SAGE-CLEAN algorithm. From the figure, we can observe that the estimation errors tend to decrease as the SNR increases, due to a higher quality signal received at a higher SNR condition, leading to better estimation accuracy. We also observe that the estimation performance improves with the number of iterations; however, this also implies a higher computational cost. In the range figure, we have also plotted the Cramer-Rao Lower Bound (CRLB) as a theoretical lower bound for parameter estimation. As we can observe, the range estimation performance gets closer to the CRLB with more iterations.

Next, we investigate the estimation performance with multiple targets. In particular, three targets are uniformly distributed in the 5 m $\times$ 5 m surveillance area. Fig. 5 illustrates the impact of the beam gap on CLEAN-SAGE estimation performance. For comparison, the corresponding estimation results using the MUSIC algorithm [12] are also displayed.

In these figures, the angle gaps between two consecutive beams are 80 % of the beamwidth and 65 % of the beamwidth, respectively. In general, a smaller angle gap leads to greater beam overlap, which can improve estimation performance. However, it could require more sectors to cover a given area, resulting in consuming more communication throughput and introducing a larger sensing delay. The search grid of the MUSIC Algorithm is set to one-tenth of the sampling interval for the delay, corresponding to 8.52 mm in range, and the angle search step is set to 0.2 degree. We observe that, for both estimation algorithms, with greater beam overlap, the precision of the angel estimation improves significantly. Another observation is that the CLEAN-SAGE has the potential to surpass MUSIC's estimation performance, particularly with additional iterations and a finer search grid.

The simulation results demonstrate that range estimation can significantly exceed the inherent limitations imposed by bandwidth and beamwidth. Adopting a 1.76 GHz bandwidth WiFi signal in conjunction with steering beams using ULAs, and relying solely on the estimated Channel Impulse Response (CIR), we achieve a range detection resolution of 8.52 cm. Moreover, the angle resolution is 5.6 degrees for the 16-element ULA, and 11.5 degrees for the 8-element ULA when the elements are spaced at 65 % of the beamwidth. With CLEAN-SAGE, super-resolution estimation can achieve sub-centimeter accuracy for range and sub-degree accuracy for angle.

Although SAGE-CLEAN can achieve super-resolution, it could result in false detection, especially when some strong

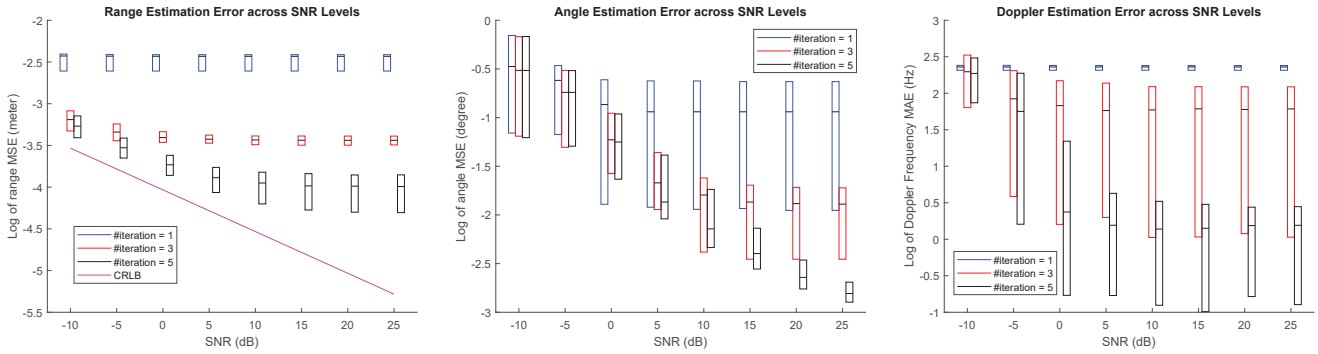


(a) (b) (c)

Fig. 4. (a) Range Estimation Error, (b) Angle Estimation Error, and (c) Doppler Estimation Error. Impact of iterative processing in the SAGE algorithm on estimation accuracy, measured across a range of SNR levels. The beam gap is 65% of the beam width, with one target randomly distributed in the designated area. A 16-element ULA is at both the transmitter and the receiver.

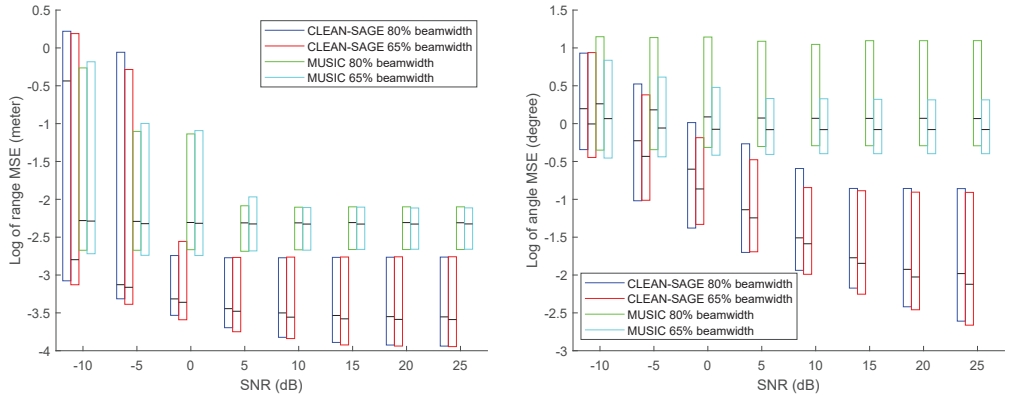


(a) (b)

Fig. 5. (a) Range Estimation Error and (b) Angle Estimation Error. Impact of the beam gap on estimation performance measured across a range of SNR levels. Three targets are randomly distributed in the designated area. A 16-element ULA is used at both the transmitter and the receiver. The SAGE algorithm employs five iterations.

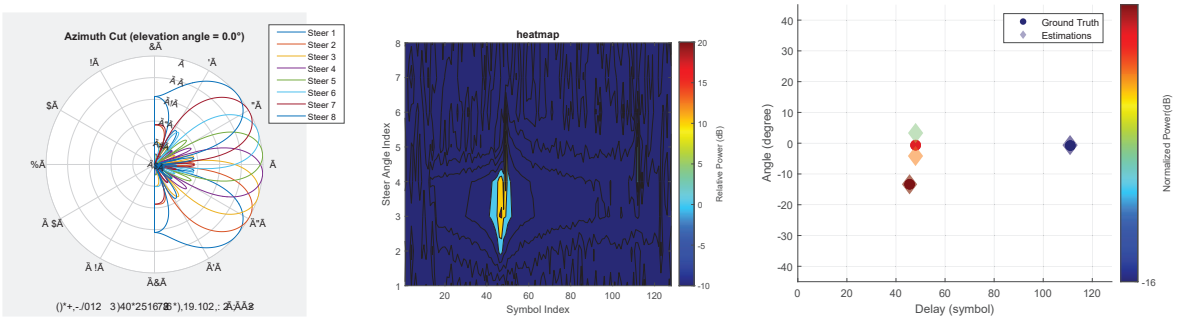


(a) (b) (c)

Fig. 6. Detection outlier using 8-element ULA. (a) Beam pattern of 8-element ULA to cover azimuth angles in the range $[-45°, 45°]$, the angle gap between two consecutive beams is 65 % of the beamwidth (b) Contour of CIRs after channel estimation, and (c) Ground truth vs. the estimation output via SAGE-CLEAN algorithm.

MPCs are spatially close to each other. Due to the greedy nature of the CLEAN-SAGE algorithm, it could result in larger estimation errors and, consequently, non-perfect cancellation. There is a risk that false alarms will happen when the signal residuals have more energy than a valid signal, as indicated in Fig. 6. In Fig. 6(c), the circles represent the ground truth, and the diamonds indicate the estimation results. There are three ground truth MPCs, two MPCs with shorter delay with much

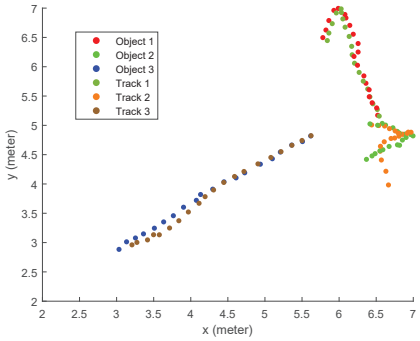


Fig. 7. Motion Tracking of Three Objects Using EKF in a 5 m $\times$ 5 m Area.

stronger power than the third MPC, and they are located within one beadwidth. Due to the side lobe of the beams and wide beamwidth, as shown in Fig. 6(a), the errors in the estimation of the two strongest MPCs lead to imperfect cancellation in the CLEAN algorithm, so the third detected MPC (the third strongest MPC) is actually a residual. Since, in our simulation, we presume that the number of signals is known, we will detect the false residual instead of the true signal, resulting in a significant error when computing the RMSE. In practice, some filtering is required. One solution is to set an energy threshold to extract all the paths above the energy threshold and use tracking algorithms to examine the MPC's trend in the time domain to remove noise or detection artifacts.

*2) Motion Tracking:* Fig. 7 illustrates the tracking results of the three moving objects in a two-dimensional space. The EKF is applied to the estimated output over time to estimate the objects' trajectory. The location data is collected at a 300 ms interval. The raw estimated objects' coordinates are depicted using distinct colors—red, green, and blue, respectively. Tracks labeled Track 1, Track 2, and Track 3 correspond to each set of estimations, colored in brown, purple, and orange, respectively. Among the three tracks, track one follows a linear movement pattern. Track two and track three display a wrap-around behavior upon reaching the area's boundary.

These tracking results demonstrate the filtered paths obtained from the EKF filter, combined with the Hungarian algorithm for associating the estimated targets with their respective tracks. The EKF assesses the dynamic state of each object over time and provides insights into the object's motion pattern, which can be important for safety applications such as robot tracking, human tracking in an indoor factory scenario, or collision detection and incident prevention in autonomous driving IoT applications.

## V. Conclusion

In this paper, we focused on a WiFi sensing scenario by leveraging the IEEE 802.11ad beamforming training procedure and designed our approach to carry out both target localization and tracking. To accurately localize the target, we explored the SAGE, an iterative method to refine parameters, combined with the CLEAN algorithm, which is used to provide the initial estimation for SAGE to achieve super-resolution estimation. We applied the super-resolution algorithm to each sector sweeping cycle. We investigated the Doppler frequency shift estimation and the feasibility of observing the channel at a sub-Nyquist rate to track the moving target effectively. We conducted extensive performance evaluations to confirm the effectiveness of our approach with the defined performance indicators.

## References

[1] J. Wang, N. Varshney, C. Gentile, S. Blandino, J. Chuang, and N. Golmie, "Integrated sensing and communication: Enabling techniques, applications, tools and data sets, standardization, and future directions," *IEEE Internet of Things Journal*, vol. 9, no. 23, pp. 23 416–23 440, 2022.

[2] K. Ngamakeur, S. Yongchareon, J. Yu, and S. U. Rehman, "A survey on device-free indoor localization and tracking in the multi-resident environment," *ACM Comput. Surv.*, vol. 53, no. 4, jul 2020. [Online]. Available: https://doi.org/10.1145/3396302

[3] N. Y. Philip, J. J. P. C. Rodrigues, H. Wang, S. J. Fong, and J. Chen, "Internet of things for in-home health monitoring systems: Current advances, challenges and future directions," *IEEE Journal on Selected Areas in Communications*, vol. 39, no. 2, pp. 300–310, 2021.

[4] H. Xu, W. Yu, D. Griffith, and N. Golmie, "A survey on industrial internet of things: A cyber-physical systems perspective," *IEEE Access*, vol. 6, pp. 78 238–78 259, 2018.

[5] H. Song, D. Rawat, S. Jeschke, and C. Brecher, *Cyber-Physical Systems: Foundations, Principles and Applications*. Academic Press, 2016.

[6] H. Jiang, C. Cai, X. Ma, Y. Yang, and J. Liu, "Smart home based on WiFi sensing: A survey," *IEEE Access*, vol. 6, pp. 13 317–13 325, 2018.

[7] Y. Ma, G. Zhou, and S. Wang, "WiFi sensing with channel state information: A survey," *ACM Comput. Surv.*, vol. 52, no. 3, Jun. 2019. [Online]. Available: https://doi.org/10.1145/3310194

[8] F. Adib, Z. Kabelac, and D. Katabi, "Multi-Person localization via RF body reflections," in *12th USENIX Symposium on Networked Systems Design and Implementation (NSDI 15)*. Oakland, CA: USENIX Association, May 2015, pp. 279–292. [Online]. Available: https://www.usenix.org/conference/nsdi15/technical-sessions/presentation/adib

[9] H.-S. Cha, G. Lee, A. Ghosh, M. Baker, S. Kelley, and J. Hofmann, "5G NR positioning enhancements in 3GPP release-18," 2024.

[10] C. D. Ozkaptan, E. Ekici, O. Altintas, and C.-H. Wang, "OFDM pilot-based radar for joint vehicular communication and radar systems," in *2018 IEEE Vehicular Networking Conference (VNC)*, 2018, pp. 1–8.

[11] P. Kumari, J. Choi, N. González-Prelcic, and R. W. Heath, "IEEE 802.11ad-based radar: An approach to joint vehicular communication-radar system," *IEEE Transactions on Vehicular Technology*, vol. 67, no. 4, pp. 3012–3027, 2018.

[12] J. Wang, J. Chuang, S. Berweger, C. Gentile, and N. Golmie, "Toward opportunistic radar sensing using millimeter-wave Wi-Fi," *IEEE Internet of Things Journal*, 2024.

[13] Y. Liu, G. Liao, Y. Chen, J. Xu, and Y. Yin, "Super-resolution range and velocity estimations with OFDM integrated radar and communications waveform," *IEEE Transactions on Vehicular Technology*, vol. 69, no. 10, pp. 11 659–11 672, 2020.

[14] F. Zhang, C. Wu, B. Wang, and K. J. R. Liu, "mmeye: Super-resolution millimeter wave imaging," *IEEE Internet of Things Journal*, vol. 8, no. 8, pp. 6995–7008, 2021.

[15] B. Smida, A. Sabharwal, G. Fodor, G. C. Alexandropoulos, H. A. Suraweera, and C.-B. Chae, "Full-duplex wireless for 6G: Progress brings new opportunities and challenges," *IEEE Journal on Selected Areas in Communications*, vol. 41, no. 9, pp. 2729–2750, 2023.

[16] J. Fessler and A. Hero, "Space-alternating generalized expectation-maximization algorithm," *IEEE Transactions on Signal Processing*, vol. 42, no. 10, pp. 2664–2677, 1994.

[17] J. A. Högbom and T. J. Cornwell, "Aperture synthesis with a non-regular distribution of interferometer baselines. commentary," *Astronomy and Astrophysics*, vol. 500, pp. 55–66, 1974. [Online]. Available: https://api.semanticscholar.org/CorpusID:116934453

[18] S. M. Kay, *Fundamentals of Statistical Signal Processing, Volume 1: Estimation Theory*. Prentice Hall, 1993.